Numerical simulations toward validating undrained conditions in Geotechnical Earthquake Engineering

David Gómez[1] Doriam Restrepo[2]

Abstract

Liquefaction denotes the loss of shear resistance of granular materials due to pore pressure build up during cyclic load. Traditionally, liquefaction is considered as an undrained phenomenon. Consequently, pore-fluid flow is deemed nonexistent during the cyclic response of sandy soils. This paper aims to shed light on the validity of this hypothesis by examining the response of natural structures made of saturated porous material subjected to vertically incident plane waves. The two porous structures, i.e., (i) an alluvial basin, and (ii) a surficial topography, are analyzed under single- and double-drainage regimes. The results are obtained using a dynamic undrained formulation and compared against an **u**-p scheme. This work provides evidence on the impact of drainage conditions, incident wavefront, frequency content, and type of natural structure, on the accuracy of the no volumetric change hypothesis. On particular, our findings show that the undrained approach exhibits a better agreement for interior topography than for surficial irregularities. Similarly, P-incident wavefronts tend to be better represented for the undrained hypothesis than SV incident waves. Finally, our results prove that the undrained approximation provides better estimates for single-drainage conditions than for double-flow regimes.

Keywords: Undrained condition, soil dynamics, pore-pressure, plane waves, drainage, alluvial basin, topography.

Introduction

Accurate predictions of the dynamic response of geomaterials continue as a major topic of research and an important matter of concern among practicing engineers. In the particular case of fully saturated cohesionless soils prone to liquefaction, such predictions become central as evidenced by the catastrophic examples of liquefaction-induced failures experienced during past earthquakes, e.g., the 1964 Niigata, Japan earthquake, and 1964 Prince William Sound, Alaska earthquake. These notorious precedents launched extensive geotechnical research during the second half of the 20th century. Performed mostly in an empirical fashion, the consensus of this early research was to deem liquefaction as an undrained phenomenon. The basic premise of liquefaction states that saturated soils are unable to develop fluid-flow when subjected to rapid cyclic loads. Since water is considered incompressible, no overall volumetric changes are generated. As a result, a densification process is triggered causing pore pressure build-up, reduction in the effective stress state, and subsequent decrease in shear soil resistance (Kramer, 1996). The dynamic undrained assumption inspired the development of a vast number of soil constitutive models, most of them aiming at predicting the behavior of sand specimens (Beaty and Byrne, 2011; Nova and Wood, 1979; Manzari and Dafalias, 1997).

[1]Graduate Student. Applied Mechanics Group at Universidad EAFIT. E-mail: jgomezz@eafit.edu.co

[2]Civil Engineering Department. Associate Professor. Universidad EAFIT. Carrera 49 No 7 Sur - 50. Medellín - Colombia. Tel.: +57 (4) 261 9337; E-mail: drestre6@eafit.edu.co

As well as an extensive amount of numerical simulations on the impact of soil liquefaction in the dynamic response of saturated granular soils (e.g., Zienkiewicz et al., 1978; Erxiang et al., 1998; Galavi et al., 2013; Bhatnagar et al., 2015; Winde, 2015).

The absence of volumetric changes, although physically justified for clay-like material where low permeability naturally constraints the seepage of internal flow, might not be entirely achieved in practice by cohesionless soils. Free surfaces where rapid gradients of pore pressure development are especially sensitive to water flow (Pande, 1982). Well-known manifestations of soil liquefaction such as sand boil, mud-spouts, or the appearance quicksand conditions at the ground surface due to seepage of water (Seed and Idriss, 1982), seem to contradict as well the zero fluid velocity postulate. Critical state theory also challenges the idea of liquefaction being an entirely undrained phenomenon. As granulated soils reduce their effective stress as a consequence of the increase pore-pressure, the stress path eventually crosses the fracture surface. In this state gaps and cracks generate, which in turn increase soil permeability, therefore allowing pore-water flow (Madabhushi and Haigh, 2012). From a thermodynamic standpoint, water incompressibility might as well drive wrong results since it leads to heating as the only mechanism for pressurization (Lakeland et al., 2014). As stated by Lakeland et al. (2014), the latter calls attention on the proper interaction of water flow, water compressibility, and thermal expansion.

Regarding the numerical analysis, the quasi-static and dynamic responses of fully saturated soils are governed by the Biot equations (Biot, 1941, 1962) The framework proposed by Biot presents the interaction between pore-fluid, solid skeleton and load rates, as the most salient feature of the dynamic regime of saturated soil porous media. As the fluid phase achieves large relative velocities about the solid phase, fluid-pressure develop. In turn, the effective stresses response of the solid skeleton changes, thus the overall system response is affected. This fully-coupled behavior is numerically considered by the discrete version of the so-called **u**-p-**U** continuum formulation (Zienkiewicz and Shiomi, 1984). Another alternative of dynamic coupling in porous media originates after rule out fluid accelerations in the overall balance equation. This approximation, traditionally known as the **u**-p formulation, has been found acceptable for most of the soil dynamic situations encountered in earthquake modeling. The dynamic undrained formulation, on the other hand, can be understood as an **u**-p scheme that neglects pore fluid velocities. Such a simplification also reduces the continuity equation allowing a direct link between pore-pressure rates and solid volumetric strain rates. Consequently, fluid pore pressure effects can be directly included in the material model of the solid constituents, therefore a single-phased representation of the porous media suffices.

Despite the simplifications mentioned above, few numerical studies tackle the validity of undrained conditions in the earthquake response of coarse-grained soils. Among them, Tasiopoulou et al. (2015) predicted the earthquake response of a multi-block gravity quay-wall according to two commercial geotechnical codes, namely FLAC (Itasca, 2005) and *PLAXIS 2D*. Numerical experiments predicted similar permanent displacements and acceleration time histories for both models. However, regarding pore-pressure development, the undrained analysis (*PLAXIS*) predicted pore pressure build up near liquefaction as a consequence of no dissipation. FLAC results, on the other hand, exhibited pore pressure values significant lower due to pore pressure migration effects. Similarly, the earthquake response of a dam model examined by Beaty and Perlea (2011) under "flow on", and "flow off" conditions exposed the significant effect of both formulations in the computed displacements. These studies, however, did not directly provide the ranges of applicability of both strategies, nor addressed the dependence of porous media response to flow conditions and seismic earthquake excitation.

This study will examine the extent to which undrained-dynamic assumptions render acceptable results in comparison with **u**-p dynamic analysis of fully saturated porous media. An irregular poroelastic basin and a topography obtained as the mirrored image of the basin interface are assumed as case studies representative of natural structures subjected to seismic loading. We examine the transient response due to the influence of vertically incident plane SV and P waves. Our simulations consider the material interface with the elastic half-space as flow-on and flow-off conditions to show the impact of flow seepage on the earthquake response.

As a first approximation, the material is considered linear. All the simulations are performed using the open source code OpenSees (Mazzoni et al., 2005).

Governing equations and finite element formulation

u-p formulation

In the absence of high frequency terms and fluid inertia, the **u**-p formulation (Zienkiewicz and Shiomi, 1984) is obtained from the equation of motion for the mixture

$$\sigma'_{ij,j} - p_{,i} + \rho b_i - \rho \ddot{u}_i = 0, \tag{1}$$

and the flow conservation equation in conjunction with the balance equation of the pore fluid,

$$\alpha \dot{\varepsilon}_{ii} + \frac{\dot{p}}{Q} + \left(\bar{k}_{ij}\left(-p_{,j} + \rho_f b_j\right)\right)_{,i} = 0, \tag{2}$$

where σ'_{ij} stands for the effective stress tensor of the soil phase, which relates to the total stress tensor according to the effective stress principle $\sigma_{ij} = \sigma'_{ij} - p\delta_{ij}$ (Terzaghi, 1943). The mass densities of the saturated mixture and pore fluid are denoted by ρ, and ρ_f respectively. b_i represents the vector of body forces. The volumetric strain of the mixture is ε_{ii}. The scaled permeability $\bar{k}_{ij}{=}k_{ij}/g\rho_f$ is expressed in terms of the soil permeability tensor k_{ij}, and the specific weight of the fluid $\gamma_f{=}g\rho_f$; g is the acceleration of gravity. Q represents the bulk compressibility of the mixture expressed in terms of the bulk modulus of the solid K_s and fluid K_f phases, the porosity η, and the parameter α, which for soils $\alpha{\approx}1$.

$$\frac{1}{Q} = \frac{\eta}{K_f} + \frac{(\alpha - \eta)}{K_s}. \tag{3}$$

In the finite element approximation the vector displacement field of the solid phase **u** and the scalar pore fluid pressure field p are expressed as interpolations of the nodal displacements $\bar{\mathbf{u}}$ and nodal pore pressures $\bar{\mathbf{p}}$ according to:

$$\mathbf{u} = \mathbf{N}_u \bar{\mathbf{u}};\ p = \mathbf{N}_p \bar{\mathbf{p}}, \tag{4}$$

where $\mathbf{N}_u$ and $\mathbf{N}_p$ are arrays of approximated shape functions. Following standard Bubnov–Galerkin ideas the weak versions of eq. (1) and eq. (2) turn into:

$$\mathbf{M}\ddot{\bar{\mathbf{u}}} + \mathbf{K}\bar{\mathbf{u}} - \mathbf{Q}\bar{\mathbf{p}} = \mathbf{f_u} \tag{5}$$

$$\mathbf{Q}^\intercal \dot{\bar{\mathbf{u}}} + \mathbf{S}\dot{\bar{\mathbf{p}}} + \mathbf{H}\bar{\mathbf{p}} = \mathbf{f_p} \tag{6}$$

where the left hand side matrices are defined as:

$$\begin{aligned} \mathbf{M} &= \int_\Omega \mathbf{N}_u^\intercal \rho \mathbf{N}_u \, \mathrm{d}\Omega; \qquad \mathbf{K} = \int_\Omega \mathbf{B}_u^\intercal \mathbf{C}_T \mathbf{B}_u \, \mathrm{d}\Omega; \qquad \mathbf{Q} = \int_\Omega \mathbf{B}_u^\intercal \mathbf{m} \mathbf{N}_p \, \mathrm{d}\Omega \\ \mathbf{S} &= \int_\Omega \mathbf{N}_p^\intercal \frac{1}{Q} \mathbf{N}_p \, \mathrm{d}\Omega; \quad \mathbf{H} = \int_\Omega (\nabla \mathbf{N}_p^\intercal) \bar{\mathbf{k}} (\nabla \mathbf{N}_p) \, \mathrm{d}\Omega; \end{aligned} \tag{7}$$

and the equivalent force vectors representing prescribed boundary conditions and body forces are,

$$\mathbf{f_u} = \int_\Omega \mathbf{N}_u^\intercal \rho \mathbf{b} \, \mathrm{d}\Omega + \int_{\Gamma_t} \mathbf{N}_u^\intercal \mathbf{t} \, \mathrm{d}\Gamma_t; \quad \mathbf{f_p} = \int_{\Gamma_q} \mathbf{N}_p^\intercal q_n \, \mathrm{d}\Gamma_q + \int_\Omega (\nabla \mathbf{N}_p^\intercal) \bar{\mathbf{k}} \, \rho_f \mathbf{b} \, \mathrm{d}\Omega; \tag{8}$$

$$\text{where } q_n = -\bar{k}_{ij}\left(-p_{,j} + \rho_f b_j\right) n_i \ ;$$

with $\mathbf{B}_u$ denoting the standard kinematic matrix, $\mathbf{C}_T$ is the tangent material constitutive model representing the effective stress-strain relation. In this study a linear material model defined in terms of the Lamé parameters λ and μ is adopted i.e., $\mathbf{C}_T = \lambda \mathbf{m}\mathbf{m}^\intercal + 2\mu\mathbf{1}$; $\mathbf{m}^\intercal = [1,\ 1,\ 0]$. $\mathbf{1}$ corresponds to the unit identity matrix, and $\mathbf{t}$ is the traction vector prescribed over the surface Γ_t . Similarly, the normal flux prescribed over the surface Γ_q is denoted as q_n (outgoing fluxes are considered negative).

Undrained dynamic formulation

If the permeability tensor approaches zero the relative velocity of the fluid with respect to the solid phase can be neglected. Consequently, the permeability matrix $\mathbf{H}$ and the flux equivalent forces $\mathbf{f_p}$ in eq. (6) vanish. The reduced continuity equation establishes a direct relation between rates of displacement and rates of pore pressure as,

$$\mathbf{Q}^\intercal \dot{\bar{\mathbf{u}}} + \mathbf{S}\dot{\bar{\mathbf{p}}} = \mathbf{0}, \tag{9}$$

since both $\mathbf{Q}$ and $\mathbf{S}$ are time independent they can be integrated (Anandarajah, 2011) yielding,

$$\mathbf{Q}^\intercal \bar{\mathbf{u}} + \mathbf{S}\bar{\mathbf{p}} = \mathbf{0}, \tag{10}$$

providing that some compressibility is allowed ($Q \neq \infty$)

$$\bar{\mathbf{p}} = -\mathbf{S}^{-1}\mathbf{Q}^\intercal \bar{\mathbf{u}}, \tag{11}$$

as a result, the discrete version of the balance equation for the mixture reduces to

$$\mathbf{M}\ddot{\bar{\mathbf{u}}} + \left[\mathbf{K} + \mathbf{Q}\mathbf{S}^{-1}\mathbf{Q}^\intercal\right]\bar{\mathbf{u}} = \mathbf{f_u}\ . \tag{12}$$

The new stiffness matrix is the so-called undrained stifness matrix $\mathbf{K_u}$

$$\mathbf{K_u} = \mathbf{K} + \mathbf{Q}\mathbf{S}^{-1}\mathbf{Q}^\intercal\ . \tag{13}$$

Since the evaluation of the term $\mathbf{Q}\mathbf{S}^{-1}\mathbf{Q}^\intercal$ is complex and time consuming, Zienkiewicz et al. (1988) presented an alternative approach to compute $\mathbf{K_u}$ as:

$$\mathbf{K_u} = \mathbf{K} + \mathbf{Q}\mathbf{S}^{-1}\mathbf{Q}^\intercal \simeq \int_\Omega \mathbf{B}_u^\intercal \left(\mathbf{C}_T + Q\mathbf{m}\mathbf{m}^\intercal\right)\mathbf{B}_u \, \mathrm{d}\Omega. \tag{14}$$

In the undrained dynamic scheme, the analysis reduces to that of a single-phase material, as long as the stiffness matrix take into consideration the bulk modulus of the mixture, while pore-pressures are dissipated by diffusion (Zienkiewicz et al., 1988).

1 Problem definition

In this section we describe the FEM simulation methodology by a set of numerical experiments performed over two idealized geological features. Namely, an alluvial basin and a topography embebbed in a homogeneous elastic half-space subject to vertically incident SV and P plane waves.
The fig. 1a illustrates a porous alluvial basin of width and maximum deep equal to $2\lambda_p$ and λ_p respectively, where $\lambda_p = V_p/f_c$ is the characteristic wavelength of the P-wave velocity, V_p is the P-wave velocity of the domain, and f_c is the characteristic frequency of the excitation. The structure is embebbed in a trunctated half space with enough dimensions such that the ocurrence of spurious reflections from the Lysmer-Kuhlemeyer absorbing boundaries do not participate in the excitation of the basin. Material damping is ommited for

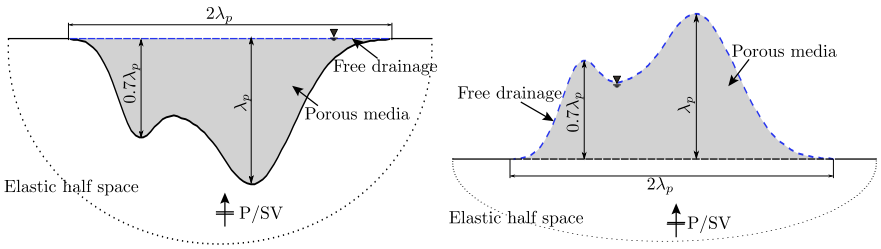

(a) Alluvial basin **(b)** Topography

Figure 1: Porous domains measures. Profiles are defined by $h(x) = (-1)^n \sum_{i=1}^{3} A_i e^{\left((x-\mu_i)^2/\sigma_i^2\right)}$, with $x \in [-\lambda_p\ \lambda_p]$, $A = \{1,\ 5/8,\ 1/4\}\lambda_p$, $\mu = \{\text{-}0.156,\ 0.556,\ 0.275\}\lambda_p$, $\sigma^2 = \{0.146,\ 0.035,\ 0.035\}\lambda_p^2$. $n = 1$ for the alluvial basin and $n = 2$ for the topography. Blue dotted line represents the free-drainage flow boundary condition imposed at free-surface on the domains.

simplicity. Similarly, fig. 1b illustrates a topography. This topography is obtained as a mirrored image of the basin. The domains are subjected to vertically incident P and SV waves. These waves allow us to remove source effects, subsequently, change are entirely generated by the saturated media, and differences among the numerical schemes. To investigate the frequency-dependent behaviour we use Ricker wavelets of unitary amplitude as seismic excitations. The displacement time history of this pulse is given by eq. (15)

$$u(t) = [1 - 2b(t - t_s)^2]e^{-b(t-t_s)^2} \tag{15}$$

where b is defined as $b = \pi f_c^2$, t_s is the surface arrival time of the wave. f_c values are used to compare the effect of the frequency content on the dynamic response of the structures: a high-frequency excitation ($f_c = 3$ Hz); a low-frequency excitation ($f_c = 1$ Hz) and an intermediate excitation ($f_c = 2$ Hz). The computational domains were discretized using a distorted quadrilateral mesh, of minimum element length according to eq. (16). Where V_s is the S-wave velocity of the discretized region, f_{max} is the maximum frequency of the incident wave, and $PPW = 10$, number of points per wavelength.

$$\Delta x = \frac{V_s}{f_{max} PPW}. \tag{16}$$

In both models the free surface is considered as a free drainage boundary. The interface of the alluvial basin with surrounding half-space, and the base of topography are analyzed under no-flux drainage (single drainage) and free drainage conditions (double drainage). Both conditions are justified by the physical evidence of the existance of pervious sand layers or unpervious clay-like materials at the bottom of the structures. Such drainage conditions are essential in unfolding the build up of pore-pressure. As a result, their consideration are essential in the comparisons proposed in this work. Table 1 describes the material parameters of the porous structures and the elastic half-space. Also, Table 2 describes the permeabilities k of the granular soils chosen in this study. These range from very permeable sands to almost impervious granular material.

Simulations are performed evaluating the $\mathbf{u}$-p formulation against a response obtained via undrained formulation with the previously defined geometrical, material and loading conditions.

Table 1: Material parameters. n is the soil skeleton porosity, K_f and ρ_f are the bulk modulus and density of pore the fluid.

	V_p (m/s)	V_s (m/s)	ρ (kg/m^3)	n –	K_f (kN/m^2)	ρ_f (kg/m^3)
Elastic half space	1200	693	1900	–	–	–
Porous media	1200	490	1900	0.25	$2.2 \cdot 10^6$	1000

Table 2: Chosen permeabilities k (m/s) . After Dysli Michel (2011), West (1995)

Tag	**Material**	$k \times 10^{-4}$ (m/s)
k_1	Clean Sand (good aquifers)	100
k_2	Alluvial sand and gravel	40
k_3	Poorly graded gravel, sandy gravel	5.35
k_4	Very fine sand	0.05
Undrained	Clayed sands	$\to 0$

2 Dynamic analysis

2.1 Time response analysis

As a first step, we explore temporal responses of the chosen domains, with the purpose of identificate overall similarities or discrepances between displacement registers given by the undrained condition U_u and the **u**-p formulation U_{up}. We analyze registers of the displacement history for two receivers at the free-surface and in the interface of the domains. The Figure 2 shows their locations. These registers are obtained from excitations of the porous domains due to P and SV vertical wavefronts at $f_c = 3$ Hz.

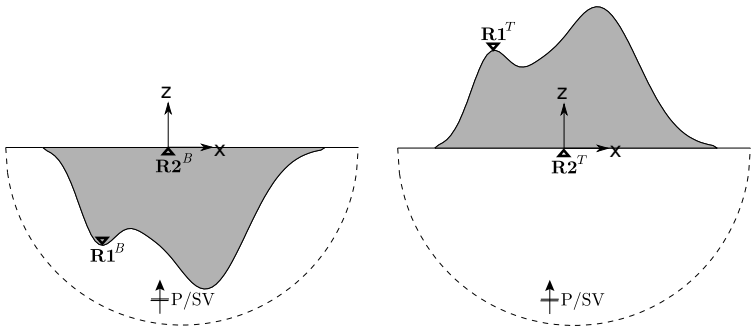

Figure 2: Locations of receivers. For the alluvial basin receivers are located at $\mathbf{R1}^B(-1/4\lambda_p, -7/10\lambda_p)$ and $\mathbf{R2}^B(0, 0)$. For the topography at $\mathbf{R1}^T$ $(1/4\lambda_p, 7/10\lambda_p)$ and $\mathbf{R2}^T(0, 0)$.

For the alluvial basin under P-wave incidence (see first two columns of Figure 3a), the response of receivers for the undrained solution coincide in good agreement with results from the **u**-p formulation. An amplification in the main peak occurs for registers solved with the coupled formulation at the highest permeability (clean sand). In contrast, for double drainage, the responses attenuate inasmuch permeability decreases. Also, the more prominent variations are shown for $\mathbf{R1}^B$, where a left shifting of the signal occurs for the undrained response. On the other hand, for SV-wave incidence (see last two columns of Figure 3a), at single- and double-drainage, the **u**-p formulation tends rapidly to the undrained response, this occurs for

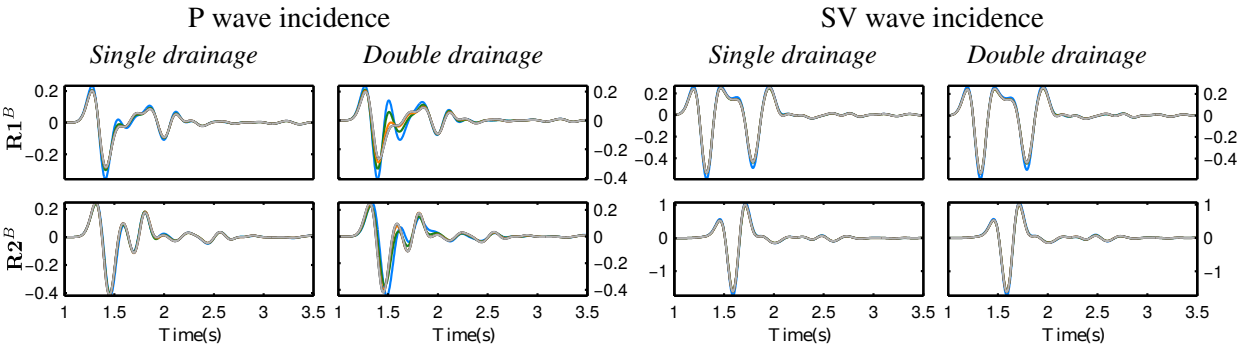

(a) Comparison of syntetics at $\mathbf{R1}^B$ and $\mathbf{R2}^B$ for the alluvial basin.

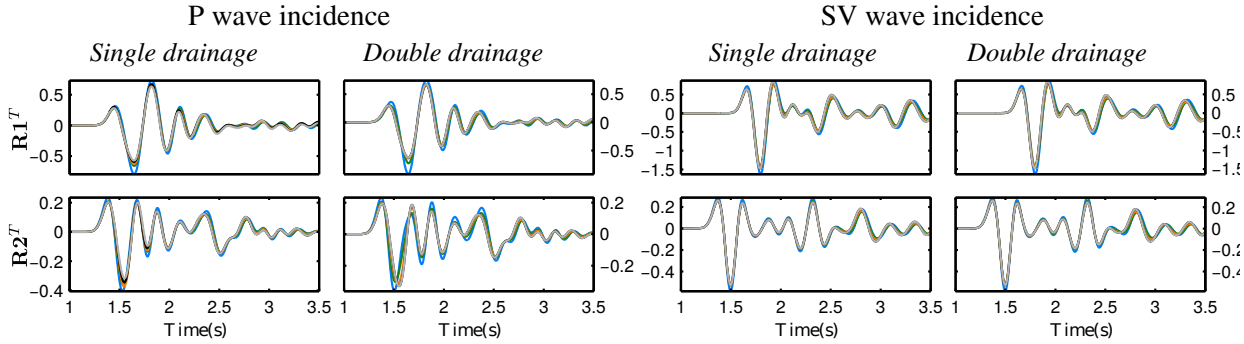

(b) Comparison of syntetics at $\mathbf{R1}^T$ and $\mathbf{R2}^T$ for the topography.

Figure 3: Comparison of the horizontal and vertical displacement (mts.) in the alluvial basin and the topography for P-wave and SV-wave incidences respectively. The column one and two for each incidence correspond to displacement's beahaviour due to single and double drainage conditions.

$k \geq$ 4E-3 m/s.

For the topography, under P-wave incidences and single drainage conditions (see first column at Figure 3b), highly permeable resposes tend to the undrained. On the other hand, signals atenuate and shift inasmuch peremability decreases (see second column at Figure 3b). Finally, for the case of SV incidence, the consideration of single and double drainage behaves in similar way.

The Tables 3 and 4 provide a quantitative assessment of $Max|\mathrm{U_u}\text{-}\mathrm{U_{up}}|$ for receivers $\mathbf{R1}^{B/T}$ and $\mathbf{R2}^{B/T}$. Notice the clear difference between assuming single and double drainage conditions for each incided wavefront in evaluated porous domains, with the more critical discrepances for the P wavefront. On the other hand, for the topography, $Max|\mathrm{U_u}\text{-}\mathrm{U_{up}}|$ measurings are 2 to 10 times greater than the obtained for the alluvial basin. Therefore, in overall, the registers for the alluvial basin achieve a more accurate fit between $\mathbf{u}$-p and undrained formulations than the topograhy registers.

2.2 The frequency analysis

To constrast the difference between the undrained condition and the $\mathbf{u}$-p formulation, we compute the free-surface transfer function for both approaches ($\mathrm{TF_u}$ and $\mathrm{TF_{up}}$ respectively) for $f_c = 3$ Hz simulations. Then, we analize the result of $\mathrm{TF_u} - \mathrm{TF_{up}}$ for different permeability values as shown in Table 2. Comparisons are performed using P and SV wavefronts at single and double drainage conditions. For the SV-wave, the TF is computed using the horizontal component of the ground motion, whereas that the vertical component is used for the P-wave case.

Table 3: $Max|U_u - U_{up}|$ for different permeability values for the alluvial basin.

	R1^B				**R2^B**			
	P wave		SV wave		P wave		SV wave	
↓ ***Tag***	*Single dr.*	*Double dr.*	*Single dr.*	*Double dr.*	*Single dr.*	*Double dr.*	*Single dr.*	*Double dr.*
k1	0.06	0.23	0.02	0.03	0.08	0.25	0.08	0.08
k2	0.02	0.15	0.01	0.01	0.03	0.13	0.06	0.05
k3	0.003	0.06	0.004	0.005	0.005	0.04	0.018	0.02
k4	3.1E-5	0.026	4.9E-5	0.002	6.75E-5	0.013	0.0002	0.003

Table 4: $Max|U_u - U_{up}|$ for different permeability values for the topograhy.

	R1^T				**R2^T**			
	P wave		SV wave		P wave		SV wave	
↓ ***Tag***	*Single dr.*	*Double dr.*	*Single dr.*	*Double dr.*	*Single dr.*	*Double dr.*	*Single dr.*	*Double dr.*
k1	0.12	0.23	0.24	0.25	0.09	0.26	0.07	0.07
k2	0.08	0.12	0.19	0.2	0.04	0.17	0.05	0.06
k3	0.04	0.05	0.09	0.09	0.013	0.07	0.02	0.02
k4	0.0007	0.01258	0.001	0.01	0.0002	0.04	0.0005	0.003

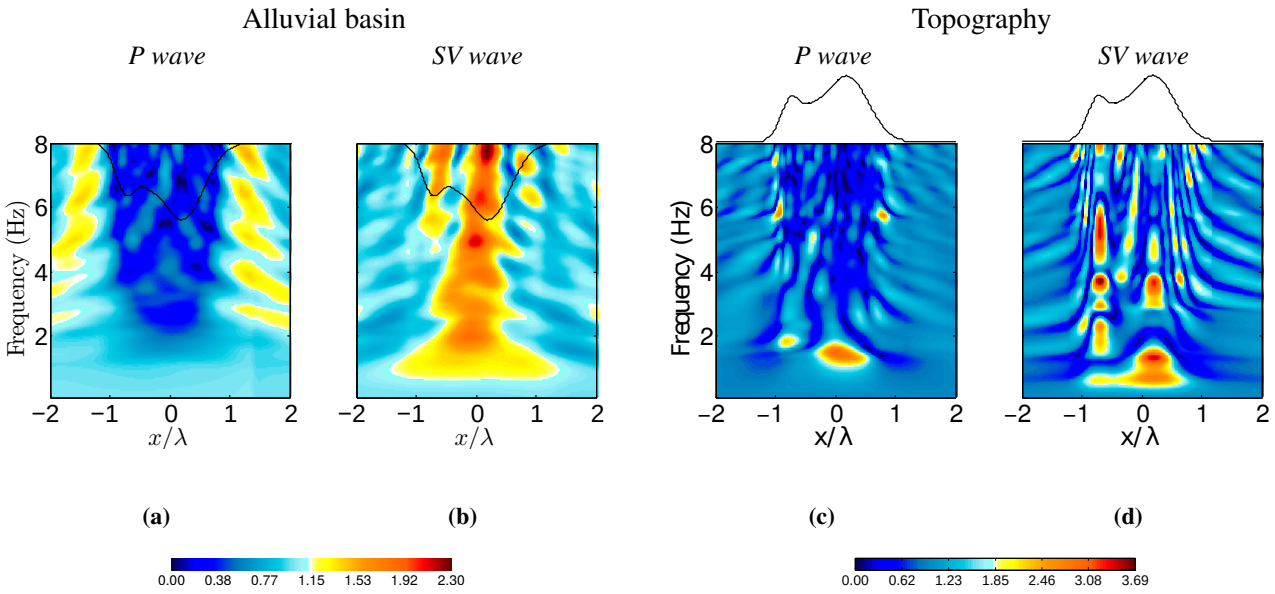

Figure 4: Free-surface transfer functions (TF) as function of position (x/λ) and frequency (Hz) for undrained free surface response on domains due to P and SV incident waves.

For the alluvial basin under P-wave, the TF_u shows deamplification patterns on the porous region (see Figure 4a) except for frequencies $0 \leq f \leq 2$ Hz. When analyzing $TF_u - TF_{up}$, the double drainage case is the most distant from its single-drainage counterpart (see Figure 5a from left to right). Here, the most remarkable variation is located at $-1 \leq x/\lambda \leq 1$, with a braid-like pattern. Also, discrepances narrow as

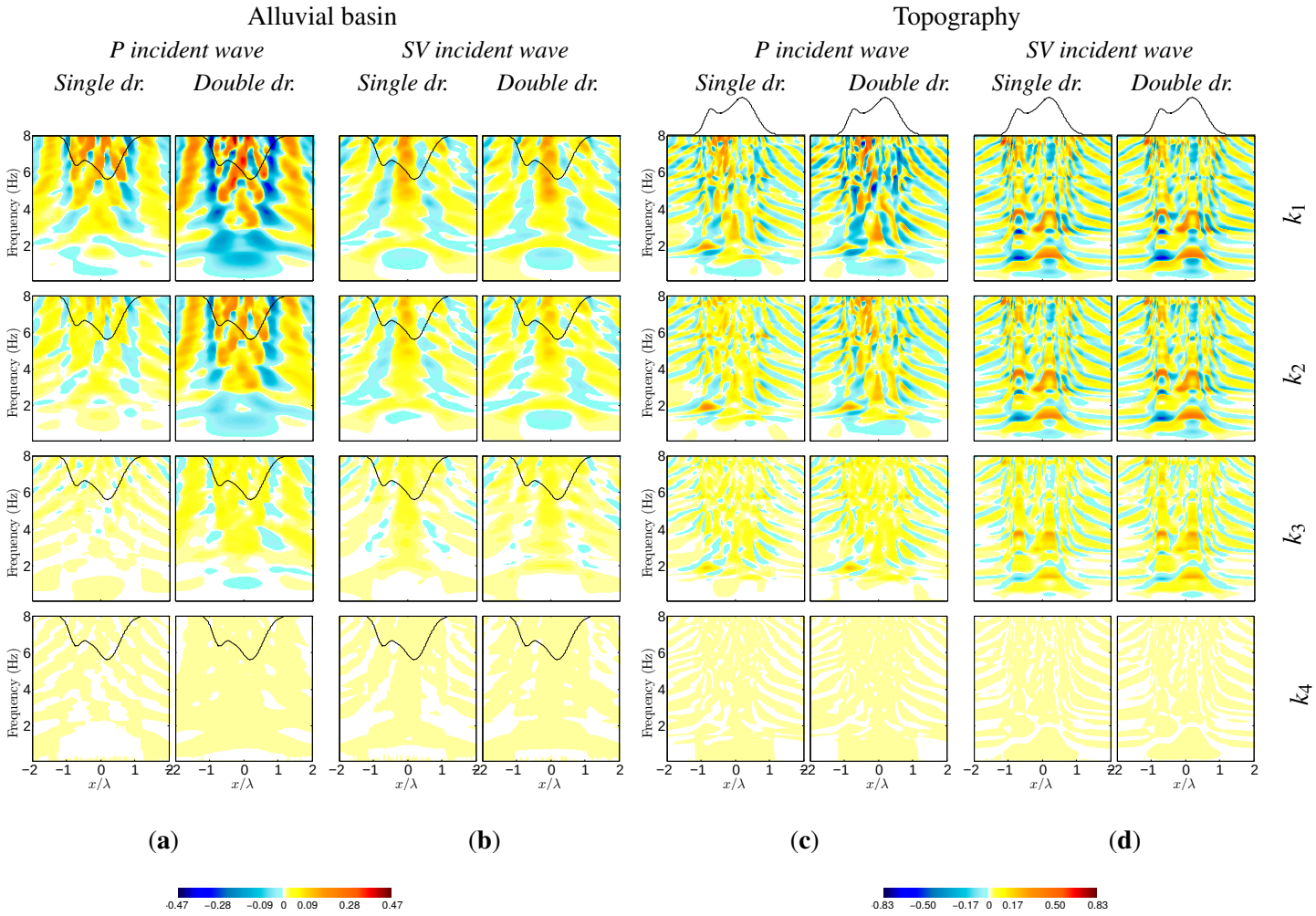

Figure 5: Difference of amplifications for porous structures against its undrained response, due to $f_c = 3$ Hz, for P and SV incident plane waves, and single/double drainage bundary conditions.

the **u**-p formulation approach to an undrained condition (see P-wave column at Table 5, and Figure 5a from above to below). For the SV-wave incidence, Figure 4b exhibits amplification patterns for all frequencies, particulary, in the main depth of the basin $x/\lambda \sim 0.5$ at $f \sim 4.5$ Hz and $f \sim 8$ Hz. On the other hand, Table 5 shows qualitative measurings which indicate that for SV incidence, there is a less prominent variation than the P-wave case between the single and double drainage conditions.

For the topograhy under P-wave, TF_u (see Figure 4c) shows at $f \sim 1.5$ Hz, an eigen mode of the structure. Two maxima of the amplification at $f \sim 6$ Hz and $f \sim 5$ Hz, are observed at mid-slope and at the valley respectively. As in the alluvial basin simulation, the double drainage shows the most remarkable variation (see Figure 5c), but surprisingly, for -single, -double drainage conditions, when $k \geq$ 4E-3 m/s, comparisons stand out amplifications of frequencies at the minor depth of the structure (see Figure 5c from above to the below). Thus, an undrained assumption is not satisfied. Finally, in $-1 \leq x/\lambda \leq 1$ response deamplificates for all frequencies as we approach to lowest permeability.

For the topography under SV-wave, TF_u (see Figure 4d) shows strong amplifications for middle and high frequencies $5 \leq f \leq 6$ Hz and $f \sim 3.5$ Hz for both summits of the domain. At low frequencies, the main eigen mode of the structure can be observed with a resonace frequency of about 1.5 Hz. No substantial

difference highlights between the obtained results for single and double drainage cases (see Figure 5c). Maximum and minimum values keep in same limits (see Table 6 at column SV wave). Finally, variations against undrained response appear where maximum amplifications are. These variations increase in the same way as permeability does (see Figure 5d).

The Tables 5 and 6 provide a quantitative assesment of $TF_u - TF_{up}$. Notice the clear difference between assuming single and double drainage conditions for each incided wavefront in evaluated porous domains. For instance, in the alluvial basin under SV wave incidence and single drainage, the difference approach since -0.0035 to 0.189 for overall permeabilities. In contrast, surficial topography under P incidence and double drainage imposes the largest differences.

Table 5: Maximum and minimum $TF_u - TF_{up}$ for different permeability values for the alluvial basin.

	P wave				**SV wave**			
	Single dr.		*Double dr.*		*Single dr.*		*Double dr.*	
↓ ***Tag***	*Min*	*Max*	*Min*	*Max*	*Min*	*Max*	*Min*	*Max*
k1	-0.26	0.28	-0.47	0.47	-0.15	0.21	-0.16	0.189
k2	-0.14	0.12	-0.3	0.25	-0.1	0.15	-0.1	0.13
k3	-0.03	0.03	-0.07	0.08	-0.03	0.05	-0.03	0.04
k4	-0.0002	0.0005	-0.0008	0.001	-0.0003	0.0005	-0.0005	0.0005

Table 6: Maximum and minimum $TF_u - TF_{up}$ for different permeability values for the topography.

	P wave				**SV wave**			
	Single dr.		*Double dr.*		*Single dr.*		*Double dr.*	
↓ ***Tag***	*Min*	*Max*	*Min*	*Max*	*Min*	*Max*	*Min*	*Max*
k1	-0.37	0.60	-0.69	0.83	-0.67	0.65	-0.72	0.61
k2	-0.22	0.4	-0.34	0.5	-0.48	0.53	-0.54	0.54
k3	-0.09	0.19	-0.093	0.23	-0.17	0.35	-0.19	0.37
k4	-0.002	0.004	-0.0018	0.005	-0.0035	0.0094	-0.004	0.01

3 The peak pore-pressure response

The maximum registered pore-pressure, refered as peak pore-pressure (PP) was interpolated for a internal curvilinear transect of the porous domains. Figure 6 shows the chosen transect as a red dotted line located at the middle of the porous domains.

For the alluvial basin under P-wave incidence, the potential of the undrained solution to accurately predict the PP response clearly depends on the drainage conditions. For single drainage for instance, the undrained solution coincide in very good agreement with results from the **u**-p formulation for the whole set of soil permeabilities examined (see tops of figures 7a, 8a, and 9a). Surprisingly, the good agreement holds for the entire length of the transect, what is indicative of basin edge effects independence. Moreover, the undrained solution correctly predicts the PP response for low and high frequency regimes. Double drainage conditions, on the other hand, limit the ability of the undrained solution to fully comply with the **u**-p results

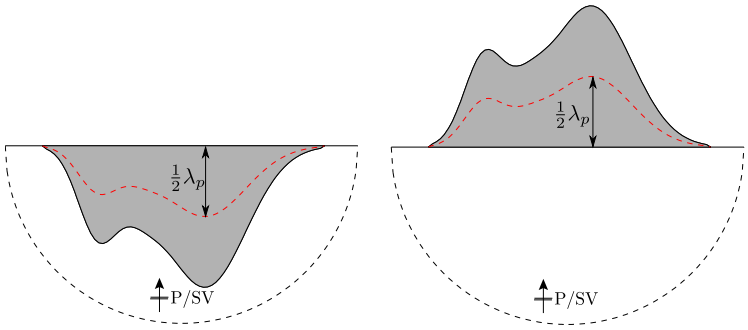

Figure 6: Curvilinear transect. The red dotted line represents the positions of receivers used to compute variations among formulations of the peak excess pore pressure (PP).

(see tops of figures 7b, 8b, and 9b). Although this effect is more prominent for soil permeabilities $k \geq$ 4E-04 m/s and receivers approaching the basin margins $|x/\lambda| \geq 0.5$. Similarly, under SV incidence, the **u**-p responses converge to the undrained solution on the middle section of the basin. Single- and double-flow regimes follow this spatial pattern of convergence (see tops of figures 7c, 7d, 8c, 8d, 9c and 9d). Near the basin edges, on the other hand, the undrained scheme still fails at reproducing the correct response for permeabilities representative of sandy gravel soils and higher. As a general trend, the undrained solution can be considered as an upper limit of the expected PP values.

The convergence of the **u**-p scheme to the undrained solution largely depends on the frequency content and type of excitation for surficial topography. At low frequencies and P-wave incidence, both techniques marginally resemble at the middle part of the topography (see bottom of figures 7a, and 7b). More important is the dramatic change in the spatial distribution pattern of PP between the undrained case and the Clean sand results (see the bottom of figure 7b). Here the uncoupled formulation displays a parabolic-like distribution of maximum peak near the middle of the transect and reducing toward the mountain feet. Conversely, the undrained simulation predicts an opposite response with the utmost values near the borders and lower PPs at the center. For low frequencies and P-wave incidence, the undrained response poorly reflects the correct distribution of excess pore pressure. Medium and high frequencies on the other hand, rapidly converge to the undrained solution (see bottoms of figures 8a, 8b, 9a and 9b). However, the bottom of figures 8a, and 8b, show that the undrained response underpredicts the PP response at $x/\lambda \sim 1/4$ for alluvial and clean sand permeabilities. The latter might lead to non-conservative assessments on the liquefaction potential at that location. SV incidence exhibits as well close agreement among the different approaches inasmuch as f_c increases (see the bottoms of figures 7c, 7d, 8c, 8d, 9c and 9d). Although, this similarity only occurs at the middle region of the transect. Near the mountain feet, there are still large differences among the undrained predictions and the **u**-p results.

Tables 7 to 9 provide a quantitative assessment on the accuracy of the undrained approximation along the transect. The data correspond to the ratio of average **u**-p excess pore water pressure to average undrained excess pore water pressure PPAv. The ratio among average fluid-pressures confirms first estimates. For instance, the alluvial basin under P wave incidence and single drainage corresponds to the simulation that is better represented by the undrained scheme. For this case the differences reach 11% for low and high frequencies, and slightly decreases to 9% at intermediate frequencies. In contrast, surficial topography subjected to SV incidence and exhibiting double drainage, imposes the largest differences among formulations. The differences decrease for medium and high frequencies, although variations as high as 13% are still present.

Figure 10 depicts the ranges of applicability of the undrained approximation. The acceptability criterion

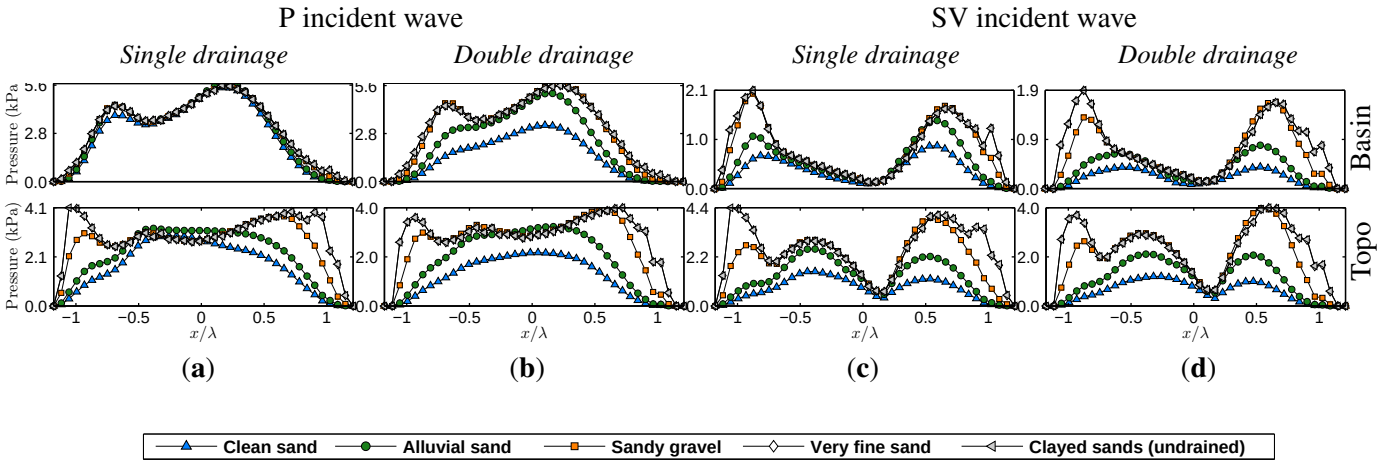

Figure 7: PP throughout the curvilinear transect shown in fig. 6, for plane vertical incidences at $f_c = 1$ Hz.

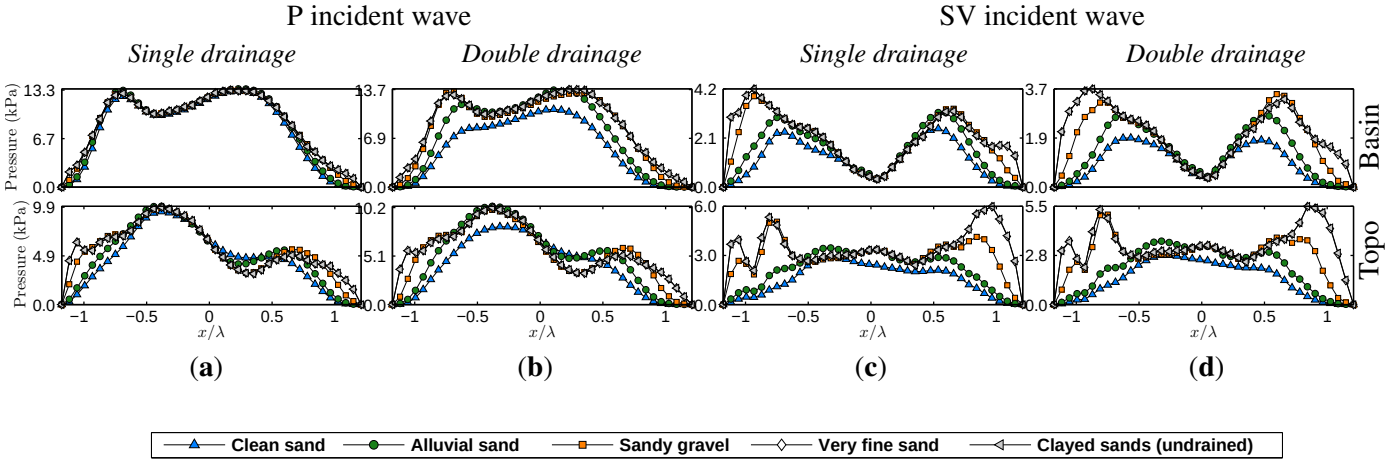

Figure 8: PP throughout the curvilinear transect shown in fig. 6, for plane vertical incidences at $f_c = 2$ Hz.

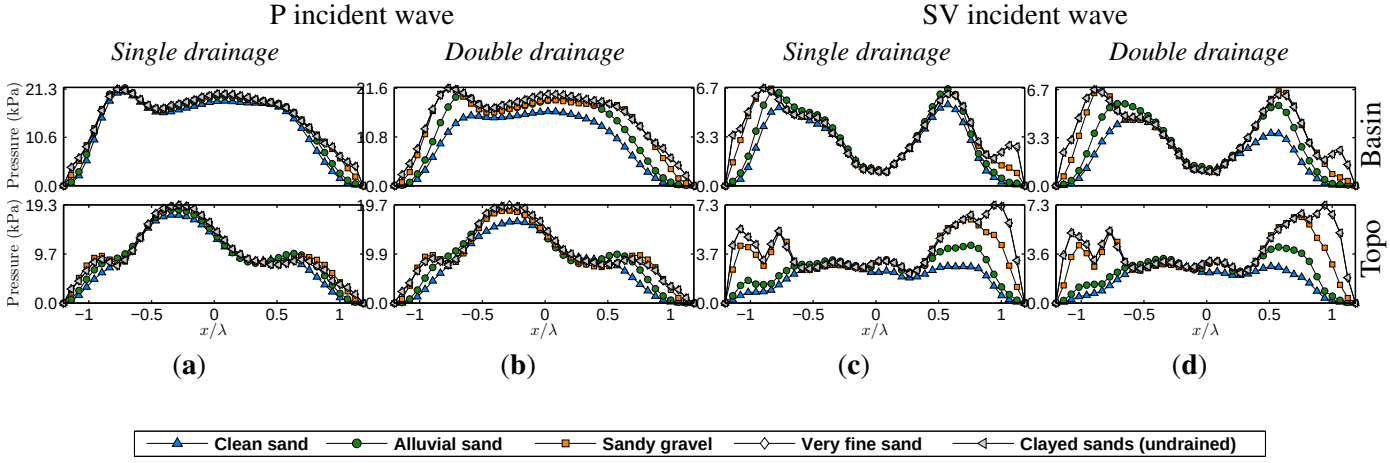

Figure 9: PP throughout the curvilinear transect shown in fig. 6, for plane vertical incidences at $f_c = 3$ Hz.

	Alluvial basin				Topography			
	P wave		SV wave		P wave		SV wave	
↓ ***Tag***	*Single dr.*	*Double dr.*	*Single dr.*	*Double dr.*	*Single dr.*	*Double dr.*	*Single dr.*	*Double dr.*
k1	0.89	0.47	0.45	0.26	0.57	0.42	0.31	0.26
k2	0.96	0.74	0.68	0.48	0.72	0.67	0.52	0.48
k3	0.99	0.97	0.95	0.86	0.89	0.91	0.84	0.87
k4	0.99	0.99	1.00	1.00	0.99	0.99	0.99	0.99

Table 7: PPAv at f_c = 1 Hz.

	Alluvial basin				Topography			
	P wave		SV wave		P wave		SV wave	
↓ ***Tag***	*Single dr.*	*Double dr.*	*Single dr.*	*Double dr.*	*Single dr.*	*Double dr.*	*Single dr.*	*Double dr.*
k1	0.91	0.63	0.58	0.47	0.84	0.73	0.47	0.45
k2	0.96	0.84	0.77	0.68	0.92	0.92	0.64	0.63
k3	0.99	0.96	0.96	0.90	0.98	0.96	0.86	0.85
k4	1.00	1.00	1.00	1.00	0.99	0.99	0.99	0.99

Table 8: PPAv at f_c = 2 Hz.

	Alluvial basin				Topography			
	P wave		SV wave		P wave		SV wave	
↓ ***Tag***	*Single dr.*	*Double dr.*	*Single dr.*	*Double dr.*	*Single dr.*	*Double dr.*	*Single dr.*	*Double dr.*
k1	0.89	0.66	0.76	0.61	0.88	0.79	0.49	0.46
k2	0.89	0.65	0.77	0.61	0.96	0.90	0.64	0.61
k3	0.99	0.94	0.96	0.93	1.00	0.96	0.89	0.87
k4	1.00	1.00	1.00	1.00	1.00	1.00	1.00	1.00

Table 9: PPAv at f_c = 3 Hz.

is based on those results from Tables 7 to 9 that present an accuracy higher than 0.95, i.e., errors $< 5\%$. In related work, Ulker and Rahman (2009) offered ranges of applicability of different formulations (undrained (**U**), quasi-static (QS), partly dynamic (**u**-p), fully dynamic) for a fixed-base, single-drainage 2D layer of saturated porous media subjected to surface harmonic loading. The model and load conditions analyzed by these authors hardly resemble those of the present study. They, however, used a more stringent error of 3% to deem a formulation acceptable. According to Fig. 10., P incidence tends to be better represented by the undrained approximation than vertically incident SV waves. Since the pore-fluid pressure in SV incoming motion can only develop after the appearing of secondary compressional waves, the undrained response predicts a greater effect from these waves due to the larger bulk modulus used. Notice that the superior performance of P wavefronts holds for internal and surficial porous topography. As expected, double drainage conditions limit the capacity of the undrained approach to providing accurate results. This conclusion is intuitive as more drainage paths increase the effects of water mobility on the response. Surprisingly, the undrained response is unfitted to comply with the error measure for porous topography and SV incidence. The accuracy of the undrained response limits to soil permeabilities $k \leq 5 \times 10^{-6}$ m/s, which are by construction representative of impervious material.

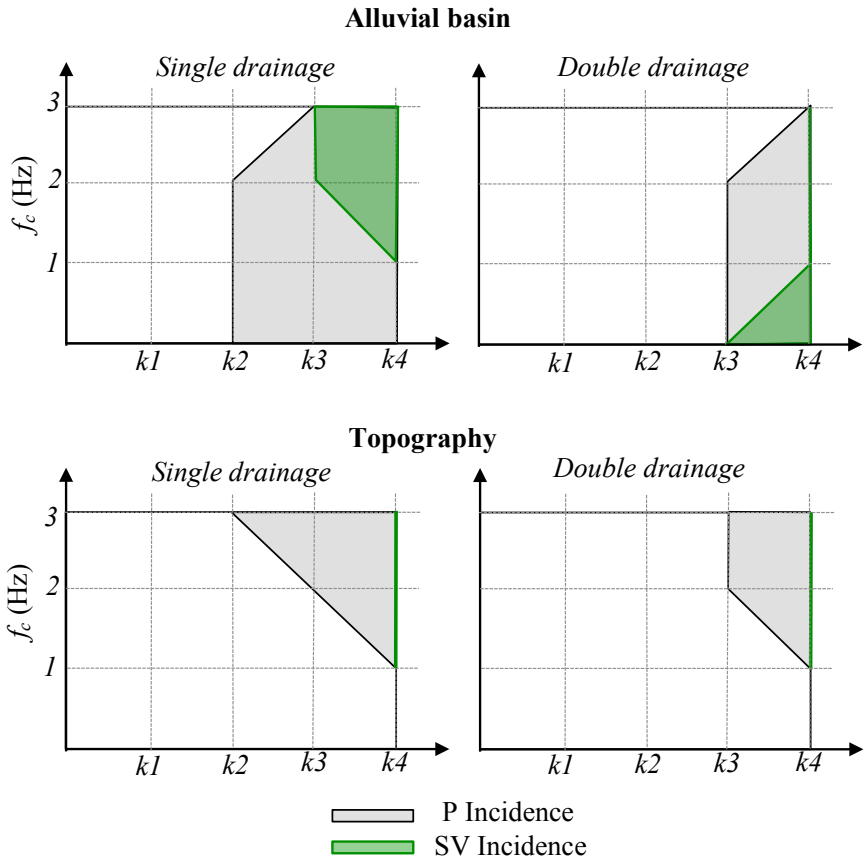

Figure 10: Ranges of applicability of the undrained approximation. The zones represent results from Tables 7 to 9 that present an accuracy higher than 0.95, i.e., errors $< 5\%$.

4 Concluding remarks

A finite elements implementation was performed using the validity of **u**-*p* formulation with the aim of asses the undrained condition in dynamic studies. A first approach was carried out through qualitative and quantitavive evaluation of the response for compressional and shear wavefields for structures prone to unfold build up of pore pressure, such as alluvial basins or topographies. In particular, the most important findings of our study are:

(i) Performed measurings, such as $Max|U_u\text{-}U_{up}|$, $TF_u - TF_{up}$ and PPAv agree that drainage conditions in the **u**-*p* formulation is a critical issue when assessing the undrained assumption in dynamic studies. Since there are more drainage paths, the less accurate overall behaviour is obtained by the undrained response. Specifically, double drainage limits the ability of the undrained solution to fully comply with the **u**-*p* formulation. Consequently, the undrained assumption is inadequate when accurately predicting dynamic phenomena where high rates of pore-pressure dissipation builds up (such as liquefaction folding), contrary as performed in the literature.

(ii) P-wave incidence tends to be better represented by the undrained approximation than SV-wave incidence. Since the pore-fluid pressure in SV incoming motion can only develop after the appearing of secondary compressional waves, the undrained response predicts a greater effect from these waves due to

the larger bulk modulus used.

(iii) Ranges of applicability of the undrained approximation were proposed for each one of the cases of study. Such regions vary in function of the flux and loading conditions, and provide an simple assessing of the undrained response against an **u**-p formulation.

(iv) Undrained approach exhibits a better agreement for interior topography than for surficial irregularities. Since it provides a wider range of applicability than the specified for the topography.

References

Anandarajah, A. (2011). *Computational methods in elasticity and plasticity: solids and porous media*.

Beaty, M. H. and Byrne, P. M. (2011). Ubcsand constitutive model version 904ar. *Documentation report: UBCSAND constitutive model on Itasca UDM Website*.

Beaty, M. H. and Perlea, V. G. (2011). Several observations on advanced analyses with liquefiable materials. In *Thirty first annual USSD conference on 21st century dam design-advances and adaptations. San Diego, California*, pages 11–15.

Bhatnagar, S., Kumari, S., and Sawant, V. (2015). Numerical Analysis of Earth Embankment Resting on Liquefiable Soil and Remedial Measures. *International Journal of Geomechanics*, 16(1):04015029.

Biot, M. A. (1941). General theory of three-dimensional consolidation. *Journal of Applied Physics*, 12(2):155–164.

Biot, M. A. (1962). Mechanics of deformation and acoustic propagation in porous media. *Journal of Applied Physics*, 33(4):1482–1498.

Dysli Michel, S. W. (2011). *Correlations in soil mechanics*. Presses Polytechniques et Universitaires Romandes (PPUR).

Erxiang, S., Zhiquan, Y., and Zonglian, Q. (1998). Nonlinear dynamic analysis of saturated soil-structure interaction by FEM. *Developments in geotechnical engineering*, 83:217–230.

Galavi, V., Petalas, A., and Brinkgreve, R. (2013). Finite element modelling of seismic liquefaction in soils. *Geotechnical Engineering Journal of the SEAGS & AGSSEA*, 44(3):55–64.

Itasca (2005). Fast Lagrangian Analysis of Continua, Minneapolis, Minnesota. *Itasca Consulting Group Inc*.

Kramer, S. L. (1996). *Geotechnical Earthquake Engineering*. Prentice Hall.

Lakeland, D. L., Rechenmacher, A., and Ghanem, R. (2014). Towards a complete model of soil liquefaction: the importance of fluid flow and grain motion. *Proceedings of the Royal Society of London A: Mathematical, Physical and Engineering Sciences*, 470(2165):1–19.

Madabhushi, G. S. and Haigh, S. K. (2012). How well do we understand earthquake induced liquefaction? *Indian Geotechnical Journal*, 42(3):150–160.

Manzari, M. T. and Dafalias, Y. F. (1997). A critical state two-surface plasticity model for sands. *Gotechnique*, 47(2):255–272.

Mazzoni, S., McKenna, F., Scott, M. H., Fenves, G. L., and Others (2005). OpenSees command language manual. Version 2.5.0. *Pacific Earthquake Engineering Research (PEER) Center*.

Nova, R. and Wood, D. M. (1979). A constitutive model for sand in triaxial compression. *International Journal for Numerical and Analytical Methods in Geomechanics*, 3(3):255–278.

Pande, G. N. (1982). *Soil mechanics, transient and cyclic loads: constitutive relations and numerical treatment*, volume 3. John Wiley & Sons.

Seed, H. B. and Idriss, I. M. (1982). *Ground motions and soil liquefaction during earthquakes*, volume 5. Earthquake Engineering Research Institute.

Tasiopoulou, P., Gerolymos, N., and Gazetas, G. (2015). Class a prediction for seismic centrifuge modeling of multi-block quay-wall: Undrained (PLAXIS) versus coupled (FLAC) effective stress analysis. In *Computational Methods in Structural Dynamics and Earthquake Engineering, COMPYD*.

Terzaghi, K. (1943). *Theoretical Soil Mechanics*. John Wiley & Sons, Inc.

Ulker, M. and Rahman, M. (2009). Response of saturated and nearly saturated porous media: Different formulations and their applicability. *International journal for numerical and analytical methods in geomechanics*, 33(5):633–664.

West, T. R. (1995). *Geology Applied to Engineering*. Prentice Hall.

Winde, H. P. (2015). Finite Element Modelling for Earthquake Loads on Dykes. Master's thesis, TU Delft, Delft University of Technology.

Zienkiewicz, O., Chang, C., and Hinton, E. (1978). Non-linear seismic response and liquefaction. *International Journal for Numerical and Analytical Methods in Geomechanics*, 2(4):381–404.

Zienkiewicz, O., Paul, D., and Chan, A. (1988). Unconditionally stable staggered solution procedure for soil-pore fluid interaction problems. *International Journal for Numerical Methods in Engineering*, 26(5):1039–1055.

Zienkiewicz, O. and Shiomi, T. (1984). Dynamic behaviour of saturated porous media; the generalized Biot formulation and its numerical solution. *International Journal for Numerical and Analytical Methods in Geomechanics*, 8(1):71–96.